Microstructure of nanocomposite wurtzite-spinel (Fe:ZnO)-(Zn:Fe3O4) epitaxial films

Xavier Portier, Christian Hébert, Emrick Briand, Jacques Perriere, Eric Millon, Christophe Cachoncinlle, Magdalena Nistor, Nathalie Jedrecy

Microstructure of nanocomposite wurtzite-spinel (Fe:ZnO)-(Zn:Fe_3O_4) epitaxial films

X. Portier[1], C. Hebert[2], E. Briand[2], J. Perrière[2], E. Millon[3], C. Cachoncinlle[3], M. Nistor[4], N. Jedrecy[2]

1 Centre de Recherche sur les Ions, les Matériaux et la Photonique (CIMAP), CEA/UMR CNRS 6252, Normandie Université, ENSICAEN, 6 Boulevard du Maréchal Juin, 14050 Caen Cedex, France.
2 Institut des Nano Sciences de Paris (INSP), Sorbonne Université, CNRS UMR 7588, 4 Place Jussieu, 75252 Paris Cedex 05, France.
3 GREMI, UMR 7344, CNRS-Université d'Orléans, 45067 Orléans Cedex 2, France.
4 National Institute for Lasers, Plasma and Radiation Physics (NILPRP), L22 P.O. Box. MG-36, 77125 Bucharest-Magurele, Romania.

Abstract

Pulsed-laser ablation of zinc and iron-based oxide targets leads to the growth on c-cut sapphire substrates of nanocomposite films constituted by randomly distributed wurtzite (Fe:ZnO) and spinel (Zn:Fe_3O_4) phases. By the complementary use of Rutherford backscattering spectrometry, X-ray diffraction and transmission electron microscopy, the nature and composition of the phases, their structure and microstructure were investigated. Both phases are textured, (0001) and (111) for the wurtzite and spinel, respectively. The epitaxial relationships with the sapphire substrate were determined: the wurtzite crystallites present the classical 30° rotation of the hexagon of their (0001) plane with respect to the hexagon of the (000l) Al_2O_3 plane. The spinel crystallites show two in-plane orientations, one corresponding to the 30° rotation of the hexagon of their (111) planes, the other one being at 0°. These two in-plane epitaxial orientations were observed for spinel crystallites directly grown on (000l) Al_2O_3 as well as for spinel crystallites inside the nanocomposite films. They are shown to be related to differences in the Zn concentration inside the spinel. A high Zn concentration (> 33%) leads to the hexagon on hexagon 0° epitaxy while a lower concentration leads to the 30° rotation. This lead us to conclude in differences in the epitaxy

of the inverse spinel (low Zn concentration in the crystallite) and of the normal spinel (high Zn concentration).

Keywords: Nanocomposite, phase separation, zinc oxide, orientation relationships, transmission electron microscopy

Introduction

Since several decades, oxide-based nanocomposite materials may be obtained in bulk form by crystallization or precipitation of a phase (metal or oxide) inside a ceramic (i.e. oxide) matrix [1, 2]. In thin film form, this approach has been explored via the phase separation [3, 4], and such a combination of simple materials revealed much better properties than each component alone [5]. Depending on the constituents and the growth conditions, nanocomposite thin films may recover multiple organization levels, ranging from small nanocrystallites embedded in a matrix [6, 7], to horizontally stacked layers or vertically aligned pillars [3, 8]. Particular emphasis has been devoted to oxide-based nanocomposite thin films consisting in self-organized vertical hetero-structures and which arise from immiscible phases, such as $BaTiO_3$-$CoFe_2O_4$ [9, 10]. The assembly mechanisms of these epitaxial oxide nanocomposite films have been presented and discussed [9].

Due to its semiconducting and piezoelectric properties, wurtzite ZnO has been used in different oxide nanocomposites [6, 11]. On the other way, spinel Fe_3O_4 or $ZnFe_2O_4$ phases have largely been studied as bulk or thin film for their magnetic properties. The ZnO-$ZnFe_2O_4$ nanocomposite in bulk or thin film form, is promising as negative electrode for lithium ion battery [12], or electrode materials for supercapacitor applications [13], for gas sensing [14], or solar photoelectrochemical water oxidation [15] and visible light photocatalytic activity [16]. Good thermoelectric properties have additionally been reported [17]. All these works evidence the importance in controlling the nature of the phases, their precise composition,

structure and microstructure, for leading to the expected physical and chemical properties. In particular, a great attention has to be paid on the cationic distribution in the different separated phases, especially concerning the spinel one which may range from Fe_3O_4 to $ZnFe_2O_4$. In that sense, the wurtzite-spinel oxide composite deserves to be studied in detail.

Starting from the wurtzite ZnO in which all Zn^{2+} are in tetrahedral position, the substitution of Zn^{2+} by Fe^{2+} leading to the $Zn_{1-x}Fe_xO$ composition may occur for $x<0.02$ ($Zn_{0.98}Fe_{0.02}O$) in air, at 800°C for bulk material [18]. In the same conditions, the insertion of Zn in the Fe_3O_4 network is more effective, as the structure is preserved with 33% of Zn^{2+} ($x = 0.66$) that corresponds to the $ZnFe_2O_4$ spinel phase. For x ranging from 0.66 to 1, a solid solution between normal and inverse spinel is formed, for which the lattice parameter follows the Vegard's law with a slight positive deviation indicating a normal structure preferably [19]. In the intermediary composition range ($0.02 < x < 0.66$), a bi-phased mixture of ZnO and $Zn_{1-y}Fe_{2+y}O_4$ ($0 \leq y \leq 1$) is obtained.

It is worth noticing that the composition ranges presented above are notably modified in thin film form. In a previous publication [20], we reported a study of the phase diagram of $Zn_{1-x}Fe_xO$ films grown by pulsed-laser deposition (PLD), by determining the nature of the phases present in the films as a function of the Fe concentration. The films were grown using a $Zn_{1-x}Fe_xO$ target, at moderate substrate temperature (500°C) and under residual vacuum (10^{-6} mbar pressure). ZnO wurtzite–based films may be epitaxially grown onto sapphire substrate down to $x = 0.35$ while pure epitaxial spinel films are formed for $x > 0.8$ [20]. The optical, electrical and magnetic properties of such wurtzite-spinel films were discussed in relation with their structural characteristics [20, 21, 22]. In the intermediate region ($0.35 < x < 0.8$), the phase separation occurs leading to both wurtzite and spinel phases. As the wurtzite lattice may contain a certain fraction of Fe, while the spinel lattice may contain a certain amount of Zn, we will use in the following the notations Fe:ZnO and Zn:Fe_3O_4 to refer to the wurtzite

and spinel phases, respectively. These nanocomposite films formed in the ($0.35 < x < 0.8$) domain were found to present electrical resistivity (from 1 to 5 10^{-2} Ω.cm) and optical properties (large absorption in a wide wavelength range) well suited to photocatalytic applications. In addition, the presence of multiple boundaries between the two phases is particularly interesting in thermoelectrics.

In the present paper, we have studied in details the texture, microstructure and epitaxial relationships of the wurtzite and spinel phases in the nanocomposite films formed in the intermediate region ($0.35 < x < 0.8$), with emphasis on the nature of the interfaces between the two oxide phases. Using X-ray diffraction and transmission electron microscopy, we have precisely determined the epitaxial relationships between the wurtzite (or spinel) phase and the c-cut sapphire substrate, and between the wurtzite and spinel crystallites inside the nanocomposite film. These relationships are discussed as a function of the variation in Zn content in the different phases and various interfaces.

Experimental

The nanocomposite (Fe:ZnO)-(Zn:Fe_3O_4) films were grown by PLD using a frequency quadrupled Nd:YAG laser ((λ = 266 nm, τ= 7 ns, 10 Hz repetition rate) in the experimental set up already described [23]. Different Zn-Fe-oxide ceramic targets with a Zn/Fe ratio equal to 0.5/0.5 or 0.6/0.4, were irradiated by laser pulses (100 mJ/cm^2). The film growth was carried out on c-cut sapphire substrates, at 500°C under 5 10^{-7} mbar, i.e. the residual vacuum. After the growth, the nanocomposite films were cooled down to room temperature under the same pressure. As previously reported [22], the nanocomposite films present excess of iron with respect to the target composition.

The film thickness and chemical composition of the films were quantitatively determined by Rutherford backscattering spectrometry (RBS), using the 2 MeV Van de

Graaff accelerator of the INSP laboratory. Such measurements gave the amount of Fe and Zn cations, with a good accuracy (1%), while the oxygen content was only determined with a 4% precision, because of the low RBS yield on light elements like oxygen. The nature of the crystalline phases present in the films was determined by X-ray diffraction analyses (XRD) using an Xpert Panalytical 4 circles diffractometer (Cu Kα radiation). The nature of the phases was investigated using the θ-2θ Bragg geometry, while the epitaxial relationships between the different phases and the c-cut sapphire substrate were determined using asymmetric diffraction, i.e. pole figure measurements.

Transmission electron microscopy (TEM) was used to characterize the local structure and composition of the films: the grain size and morphology, the orientation relationships between the substrate and the grains as well as those between the stacked grains, and the local chemical compositions of the grains and interfaces. The microscope used was a double corrected JEOL ARM 200F cold FEG operated at 200 kV, equipped with an energy dispersive X-ray (EDX) spectrometer (CENTURIO set up from JEOL) and an electron energy loss spectrometer (EELS, GIF QUANTUM 965ER setup from GATAN). The microscope was also implemented with a scanning system (STEM) combined with HAADF JEOL and GATAN detectors. The spatial resolution was 1 Å in TEM and 0.8 Å in STEM-HAADF mode. All the images were recorded and analyzed with the commercial software from GATAN called DIGITAL MICROGRAPH (DM2 version). The TEM foils were prepared by Focused Ion Beam (Helios Dual Beam nanolab660 FIB system). To protect the film surface from the gallium ion beam induced damage, a protective carbon layer and two platinum layers (one deposited electronically and the other one with the Ga beam) were deposited on the sample's surface prior to the thinning process.

Results

Chemical composition and microstructure of the nanocomposite films

Different nanocomposite films with wurtzite and spinel phases were obtained for a Fe/(Fe+Zn) ratio x between 0.50 and 0.75. We recall here that while the wurtzite phase is always present for x lower than 0.80 [20], its presence is negligible for higher Fe concentrations (the Zn:Fe_3O_4 spinel phase is only formed). The phase separation leading to the presence of both wurtzite and spinel also depends upon the oxygen pressure during the growth, as observed in other cases [4]. Indeed, in Fe_3O_4 the O/Fe ratio is equal to 1.33, and this means that an O/Fe ratio close to this value must be reached for the formation of the spinel phase. A too high ratio would lead to the formation of Fe_2O_3. In this work, the phase separation was obtained in the $5\ 10^{-7}$ to $5\ 10^{-6}$ mbar oxygen pressure range.

A typical RBS spectrum of a (Fe:ZnO)-(Zn:Fe_3O_4) nanocomposite film is shown in Fig. 1. The RUMP simulation program was used to obtain the concentration profile of the elements. The experimental spectrum cannot be fitted using an homogeneous composition. The simulated curve (continuous line) on the spectrum is obtained considering a Zn enrichment (or Fe depletion) towards the film-substrate interface, i.e from $Zn_{0.23}Fe_{0.77}$ composition at the top surface of the film, towards $Zn_{0.26}Fe_{0.74}$ at the interface with the substrate. The origin of this difference may be either an inward diffusion of Zn towards the interface or an outward Fe diffusion towards the surface during the film growth. This last possibility has been observed in the case of annealing at 700°C of Fe implanted in ZnO crystal with formation of the spinel phase [24].

Figure 2(a) is a bright field TEM image of a nanocomposite film taken along the [01-10] (or [120]) direction of the sapphire substrate. Large elongated grains are lying parallel to the film/substrate interface, i.e. the nanocomposite looks like a random stacking of crystallites. Various contrasts are clearly visible from one grain to another. They correspond mainly to

orientation changes (Bragg contrast) and/or composition variations (Z contrast). Another explanation could be the variation in the foil thickness due to the FIB system using a Ga beam for the thinning process but such a phenomenon would have led to lines and trenches in the image from the top to the bottom since the thinning process is unidirectional. Contrast variations are also visible in the grains. They are more likely explained by local strains modifying the Bragg conditions in these regions and may be by some local concentration fluctuations. Most of the grain boundaries are not sharp despite the good texture of the film with respect to the substrate. Figure 2(b) is a STEM HAADF image of a different region of the film than that presented in Fig. 2(a), and showing a clear variation in the chemical contrast from grain to grain. The whiter regions are richer in the heaviest element (Zn). Figures 2(c), (d) and (e) are STEM EDX images (chemical maps) for Zn, O and Fe respectively using their K edges. The oxygen map has a uniform contrast whereas the Zn map reveals some brighter regions indicating an enrichment of Zn especially close to the substrate and at junctions between large grains. The Fe map shows a Fe deficiency where a higher Zn content is observed. This result suggests that most of the grains are Zn:Fe_3O_4 with only a few small elongated Fe:ZnO ones located at the film/substrate interface and between large spinel crystallites.

Typical X-ray diffraction diagrams of nanocomposite films with x values of about 0.60 and 0.75 are presented in Fig. 3. In each case, two characteristic peaks related to the two phases, i.e. the 0002 reflection from the (hexagonal) wurtzite phase and the 222 reflection from the (cubic) spinel phase are observed, attesting the preferential texture for these two phases. Except these two peaks, only the 111 and 333 reflections from the spinel phase (and the 0003 and 0006 reflections from the substrate) are present when scanning on a larger 2θ angular range (10-60°, not shown). For the wurtzite phase, the 0002 peak is broad and shifted towards lower 2θ values than that of bulk ZnO, indicating an increase of the c-axis parameter.

This increase has been already observed [20, 25], and it can be related to the presence of Fe^{3+} ions in substitution of Zn in the wurtzite matrix [25]. The broadening of this peak can be due to both the large variation in the Fe concentration in the wurtzite phase, and the small size of the wurtzite crystallites. On the contrary, the position of the 222 spinel peak is well defined and its FWHM does not change with the film composition. In fact, the Zn doped ferrite is thermodynamically stable up to high Zn concentration (33%), and the variation of the spinel parameter with the Zn content is rather low. At last, the sharpness of the 222 peak of the spinel phase is consistent with the larger spinel grain size.

Epitaxial relationships of the wurtzite and spinel phases on sapphire

The wurtzite and spinel phases are both textured, and their in-plane epitaxial relationships have been determined by pole figure measurements. Figure 4 represents typical pole figures recorded for the wurtzite (Fig. 4(a)) and spinel (Fig. 4(b)) phases. The pole figure (Fig. 4(a)) was obtained with the 10-11 Fe:ZnO reflection at $2\theta = 36.25°$, and 12 poles are observed in this figure. They correspond to two series of 6 poles which are attributed to (i) the 10-11 Fe:ZnO poles (indicated by *) at a declination angle $\Psi = 61.80°$, and (ii) the 311 Zn:Fe_3O_4 poles at $\Psi = 58.50°$. The 2θ value in this latter case is equal to 35.30°, i.e. a value sufficiently close to the diffraction angle of 10-11 Fe:ZnO, to give a contribution in the pole figure. The azimuthal position of the six 10-11 Fe:ZnO poles with respect to the sapphire substrate leads to the following in plane epitaxial relationship :

Fe:ZnO [2-1-10] (or [100]) // Al_2O_3 [10-10] (or [210]) W-30°

This relationship corresponds to a 30° rotation of the hexagons of the (0001) Fe:ZnO wurtzite lattice plane with respect to the hexagons of the (0001) Al_2O_3 lattice plane, and it will be noted by hereafter W-30°. This is the classical epitaxial relationship observed for pure ZnO films grown on c-cut sapphire substrate at $T \geq 500°C$ [26, 27]. This epitaxial relationship was

always observed, whatever the Fe concentration in the wurtzite phase, when this phase was present. The comparison of the respective in-plane lattice spacing for the [10-10] (or [210]) sapphire and [2-1-10] (or [100]) wurtzite directions shows a very large lattice mismatch [28]. In the frame of the domain matching epitaxy [28, 29] such a W-30° in plane orientation is explained by the coincidence of m lattice units of the substrate with p lattice units of the film. The m and p values are defined as the minimum integers satisfying the relation: $md_s = pd_f$, where d_s and d_f are the respective atomic distances in the substrate and film parallel directions [29, 30]. In the present case, along the [10-10] (or [210]) axis of sapphire it comes that (m = 7, p = 6) leads to a lattice mismatch δ = 1.41 % and a minimum size of epitaxial domain D equal to 34 Å, as indicated in Table I which presents the matching relationships, lattice mismatch δ and size of epitaxial domain D, for the various epitaxial relationships evidenced in this work.

In Fig. 4(b), the pole figure was recorded for the 220 spinel reflection at 2θ = 29.80°. Twelve poles are observed at Ψ = 35.60°, and they correspond to two series of 6 poles which characterize different epitaxial relationships. The first one (indicated by #) corresponds to the following in-plane epitaxial relationship with the sapphire substrate:

$$Zn{:}Fe_3O_4\ [10\text{-}1]\ //\ Al_2O_3\ [10\text{-}10] \text{ or } [210] \quad S\text{-}30°$$

This relationship also corresponds to a 30° rotation of the hexagons of the (111) spinel plane with respect to the hexagons of Al_2O_3, and it will be noted by S-30°. Notice that in the (111) lattice plane of the spinel, the lattice parameter is equal to $a_c/\sqrt{2}$ where a_c is the parameter of the cubic cell. The S-30° orientation has already been observed in the case of a single-phase $Zn{:}Fe_3O_4$ film on sapphire substrate, with high Fe concentrations (> 0.80) and for which, the wurtzite phase is not present [20]. For this S-30° epitaxial relationship, as reported in Table I,

the lattice mismatch corresponds to m = 7 and p = 5, leading to a lattice mismatch δ = 0.9% and a minimum size of epitaxial domain equal to 42 Å.

The 6 other poles in Fig. 4(b), correspond to the following epitaxial relationship:

$Zn:Fe_3O_4$ [10-1] // Al_2O_3 [2-1-10] (or [100]) S-0°

In this case, the hexagons of the (111) oriented zinc ferrite spinel crystallites have the orientation of the hexagons in the (0001) plane of Al_2O_3, i.e. the "hexagon on hexagon" orientation, which will be noted by S-0°. For this epitaxial relationship, 4 zinc ferrite units and 5 sapphire units are matching with a very low value of lattice mismatch δ equal to 0.15% (Table I).

The presence of two series of poles in Fig. 4(b), means that two kinds of (111) spinel crystallites are present in the nanocomposite film. Looking more precisely at the 6 poles of the S-0° epitaxy, it appears that 3 of these 6 poles are more intense than the others. Actually, the azimuthal positions of these 3 poles are exactly the same as those of the 10-11 poles of the Al_2O_3 substrate (not shown in the figure). These 3 poles correspond thus to spinel crystallites with (111) planes presenting a three-fold symmetry, as it is the case for the (0001) planes of Al_2O_3. The other poles have presumably the six-fold symmetry. Two kinds of S-0° spinel crystallites would thus be present: (i) with a three-fold symmetry, and (ii) with an apparent six-fold symmetry.

In addition, a detailed analysis of the six S-0° poles in Fig. 4(b) shows that these poles present symmetric shoulders in their azimuthal positions, i.e. at about 10/11° with respect to the central pole position. The following in-plane epitaxial relationships can explain the presence of these shoulders:

$Zn:Fe_3O_4$ [11-2] // Al_2O_3 [41-50] (or [320]) S-11°

This in-plane orientation which is noted S-11°, corresponds to the coincidence of 5 Al_2O_3 lattice unit with 6 zinc ferrite lattice units, leading to a -1.9 % lattice mismatch and D = 62 Å for the minimum epitaxial domain (Table I). Although this lattice mismatch is largely higher than that for S-0° (- 0.15%), zinc ferrite crystallites can be grown following this orientation.

Relative orientations and compositions of the wurtzite and spinel crystallites

The above analysis has allowed the determination of the specific orientations of the various crystallites with respect to the sapphire substrate. However, the nanocomposite nature of the films has to be taken into account. Actually, TEM images of the films show that in addition to wurtzite and spinel crystallites directly grown on Al_2O_3, crystallites inside the film present specific relative in plane orientations. A typical example is presented in Fig. 5 which shows an HRTEM image where Fe:ZnO and Zn:Fe_3O_4 successive crystallites following the growth direction are observed. The fast Fourier transforms (FFT) are also shown for each crystallite. Starting from the c-cut sapphire substrate, the following epitaxial crystallites are found:

- a wurtzite crystallite with the as-expected W-30° orientation,

Fe:ZnO [2-1-10] (or [100]) // Al_2O_3 [10-10] (or [210])

- a spinel with a S-0° orientation (with respect to the sapphire substrate) meaning that this crystallite is 30° rotated with respect to the underneath W-30° wurtzite crystallite

Zn:Fe_3O_4 [11-2] // Fe:ZnO [2-1-10] (or [100])

- a spinel with a S-30° orientation, meaning a 30° rotation with respect to the underlying S-0° spinel crystallite

Zn:Fe_3O_4 [10-1] // Zn:Fe_3O_4 [11-2]

- a wurtzite crystallite with a W-30° orientation on a S-30°, i.e. hexagon on hexagon with respect to the underlying spinel crystallite

Fe:ZnO [2-1-10] (or [100]) // Zn:Fe_3O_4 [10-1]

- a S-0° spinel crystallite with a 30° rotation with respect to the wurtzite, as previously observed.

The matching relationships, lattice mismatch and the minimum domain size corresponding to these epitaxial relationships are given in Table I. Regarding the domain sizes, it is not obvious to compare directly the data provided by the XRD data and those observed by electron microscopy. However, one can notice that the dimensions of the grains perpendicular to the film shown in the HRTEM image in Fig. 5 are of the same order of magnitude than those reported in Table 1.

The poles figures (Fig. 4) and TEM image (Fig. 5), agree with the fact that the wurtzite phase shows a sole in-plane orientation (W-30°). Actually, these W-30° wurtzite crystallites are grown directly on Al_2O_3, or inside the film, on spinel crystallites presenting the S-30° orientation. The (W-30° on S-30°) epitaxy, which corresponds to a hexagon on hexagon scheme, is indeed favored by a low lattice mismatch (δ =0.3%) together with a low domain size (D =36 Å), while the (W-0° on S-30°) epitaxy would lead for equivalent δ to a domain size of at least 100 Å.

On the contrary, the spinel phase may present different in-plane orientations. The S-30° orientation is observed for spinel crystallites grown on spinel crystallites (S-0°) (Figure 5), and also on the c-cut sapphire substrate (Figure 6). Both epitaxies may be explained (Table I) by a low lattice mismatch associated to a low domain size; on spinel, two possibilities are given: a relatively high lattice mismatch (1%) with a low domain size (42 Å), and secondly a low mismatch (0.3%) with a high domain size (114 Å).

The in-plane orientation S-0° is observed for spinel crystallites grown either on Al_2O_3 (Figure 6), or on W-30° wurtzite crystallites inside the film (Figure 5). The corresponding very low lattice mismatch (δ = - 0.05%) and low domain size (D = 62 Å) of this epitaxial orientation explain its presence. The epitaxial growth of (111) oriented ferrite or Zn-doped ferrite on (0001) ZnO has already been reported [24], and a 30° in-plane rotation has been observed, in agreement with our results. Moreover, since the W-30° wurtzite presents a six-fold symmetry, it comes that the spinel crystallites growing on them with the S-0° orientation will present the same symmetry in the pole figure, i.e. a six-fold symmetry. It can thus be concluded that the S-0° crystallites presenting the three-fold symmetry in the pole figure would correspond to crystallites directly grown on the Al_2O_3 substrate.

The S-11° orientation relationship is more complicated to interpret. A possible explanation could be the result of stress between well oriented grains during the film growth but deeper investigation is needed to elaborate a possible formation mechanism.

Concerning the origin of the S-0° and S-30° orientations of the spinel crystallites directly grown on the Al_2O_3 substrate, the comparison of the associated lattice mismatch and domain size (Table I) indicates that the S-0° would be the more favorable case. Our TEM results show that the most frequently observed is the 30° rotation for the spinel phase, the S-0° usually appearing when the wurtzite phase is present, i.e. for sufficient Zn concentrations. Additional insights have been obtained through the analysis of the Zn and Fe composition of the spinel crystallites. Figure 6 shows HRTEM images and EDX atomic profiles corresponding to S-30° and S-0° crystallites directly grown on Al_2O_3. For the S-30° orientation (Figures 6(a) and (b)), the EDX profiles indicate a constant concentration of Fe and Zn, through the whole spinel crystallite. The cationic distribution $Zn_{0.21}Fe_{0.79}$ as deduced from these EDX profiles must be compared to the overall distribution obtained by RBS, that

is $Zn_{0.25}Fe_{0.75}$. A slight deficit in Zn exists in the S-30° crystallites, which can be related to the presence of the wurtzite phase in the nanocomposite film.

Differently, for the S-0° spinel crystallite, a Zn enrichment is observed at the interface with the substrate, accompanied by a corresponding decrease of the Fe content (Figures 6(c) and (d)). The cationic distribution deduced from EDX in the region close to the interface with the substrate is $Zn_{0.39}Fe_{0.61}$ (to be compared to $Zn_{021}Fe_{0.79}$ for S-30°). This corresponds to a spinel highly rich in Zn, with the composition $Zn_{1.17}Fe_{1.83}O_4$. This behavior was systematically observed in the case of spinel crystallites directly grown on the sapphire substrate with the S-0° orientation, and would mean that above a certain increase in the Zn concentration in the zinc ferrite, a change in the in-plane epitaxial relationship with the c-cut sapphire substrate will occur (from S-30° to S-0°). The driving force for the S-0° orientation would thus be the Zn enrichment at the interface with the substrate.

Similar phenomena can be observed when the wurtzite phase is present. Indeed, Fig. 7(a) shows an HRTEM image of a region with a rather thin wurtzite layer (about 8 nm thick) between the substrate and a S-0° oriented spinel. The EDX analysis (Fig. 7(b)) leads to a $Zn_{0.5}Fe_{0.5}$ cationic distribution in the wurtzite crystallite, followed by a decrease of the Zn concentration in the spinel phase. The S-0° oriented spinel phase is related to the high Zn concentration at the interface with the wurtzite crystallite, since in the "bulk" of the S-0° spinel crystallite, a $Zn_{0.2}Fe_{0.8}$ cationic distribution is present. In the case of two spinel crystallites separated by a wurtzite crystallite (Figures 7(c) and (d)), the presence of the wurtzite crystallite leads also to a change in the spinel orientation. In the middle part of the image in Fig. 7(c), the wurtzite presents the "hexagon on hexagon" orientation with respect to the S-30° spinel crystallite underneath. In the upper part, the spinel (S-0°) presents a 30° rotation with the wurtzite W-30°. The EDX scan in the middle part of the image (Fig. 7(d)) shows a general increase of the Zn concentration (on average $Zn_{0.5}Fe_{0.5}$) as expected for the

wurtzite phase formation (W-30°) on the S-30° spinel phase. A steep decrease of the Zn concentration is noticed at the interface with the S-0° spinel, together with a sharp interface, compared to the case of the interface with the S-30° spinel.

Discussion

The above results show well-defined epitaxial relationships between the wurtzite and spinel phases and the Al_2O_3 substrate. These specific in-plane orientations are directly related to changes in the Zn concentration in the spinel crystallites. Magnetite Fe_3O_4 is an inverse spinel, where the tetrahedral sites are occupied by Fe^{3+} while the octahedral sites contain Fe^{2+} and Fe^{3+} ions. On the contrary, $ZnFe_2O_4$ is a normal spinel, the octahedral sites being occupied by only Fe^{3+} ions. The occupancy of Zn^{2+}, Fe^{2+} and Fe^{3+} cations in octahedral or tetrahedral sites is governed by ionic size effect and preferred environment related to crystal field. It has been calculated that the site preference of Zn^{2+} is in tetrahedral geometry [31]. The following reaction:

$$Zn^{2+}_{octa} + Fe^{3+}_{tetra} \rightarrow Zn^{2+}_{tetra} + Fe^{3+}_{octa}$$

is exothermal (-5.02 kJ at 900°C) [31]. This reaction may occur when iron atoms in pure magnetite are substituted by Zn^{2+}. It comes that a cationic exchange from Fe^{2+}_{octa} and Fe^{3+}_{tetra} in magnetite allows to insert Zn^{2+} in tetrahedral sites in magnetite leading to switch to the normal spinel structure of zinc ferrite. The S-0° orientation would thus correspond to the epitaxial growth of normal spinel (Zn rich) on the c-cut Al_2O_3, while the S-30° orientation would correspond to the epitaxial growth of inverse spinel on the sapphire.

The S-0° oriented crystallites present a three-fold symmetry in the pole figure of Fig. 4(b), while the S-30° crystallites lead to a six-fold symmetry in this pole figure. Such a, i.e. the existence of crystallites presenting different symmetries in the pole figure has been

previously reported in the case of the growth of In_2O_3 bixbyite films on c-cut sapphire substrate [32]. This was interpreted assuming that "ordered" and "disordered" bixbyite crystallites were present in the films, the "disordered" crystallites having a random distribution of oxygen vacancies in their (111) planes leading to a six-fold symmetry. Differently, a fixed distribution of oxygen vacancy in this plane led to the three-fold symmetry of the ordered bixbyite crystallites. A similar approach can be proposed here, based on the fact that Zn is randomly substituted to Fe in tetrahedral sites of the spinel lattice [33]. If these Zn ions occupy fixed lattice positions in the (111) planes, an ordered crystallite with a three-fold symmetry would be obtained. On the contrary, if the Zn ions are randomly distributed in the tetrahedral sites of the (111) planes, a disordered crystallite with a six-fold symmetry will be obtained.

In the epitaxial growth of a film on a substrate, the nature of the first plane on the film grown on the substrate is of prime importance. Indeed, the precise atomic repartition in this plane will define the interface energy which will play a major role in the epitaxial relationships between film and substrate. The (000l) plane of the sapphire substrate is a polar plane, and in the growth conditions the last sapphire plane would be an oxygen plane [34, 35]. Accordingly, the first plane of the growing zinc ferrite would be a cationic plane. In the spinel structure, two kinds of cationic (111) planes are present: one is named the Kagomé plane (K plane) with a specific site distribution [35, 36], and the other one presents a triangular network (T planes). Moreover, the K plane only contains octahedral sites, while two different T planes are identified containing either only tetrahedral sites (Tt planes), or only octahedral sites (To planes). In the spinel structure, the (111) planes distribution is the following: K-Tt-To-Tt-K [36]. In the case of a low Zn concentration in the crystallites (corresponding to the S-30° epitaxy), both Zn and Fe will be present in the Tt planes (inverse spinel). Assuming that the Zn and Fe are randomly distributed in such Tt planes, this will lead to a six-fold symmetry for

such crystallites. Differently, for a high Zn concentration (corresponding to the S-0° epitaxy), Zn will occupy the sites of the Tt planes (normal spinel), and a three-fold symmetry is possible for such high Zn concentration crystallites. It follows that a Tt plane would be the first plane on the sapphire for the S-0° epitaxy.

Then, it seems reasonable to assume that the S-30° epitaxy would correspond to a Kagome plane as the first plane on the sapphire substrate for the crystallite with a low concentration in Zn. Indeed, the triangular planes Tt and To present the same site distribution, even if these sites are occupied be different cations (Zn or Fe), and they would correspond to the S-0° epitaxy.

These nanocomposite films formed during this work, look like the random stacking of wurtzite and spinel platelets with variable thicknesses, i.e. 5 to 15 nm for the wurtzite and 5 to 30 nm for the spinel phase. The formation of the wurtzite platelets is *a priori* not expected. Indeed, the pure ZnO phase classically presents a c-axis texture with a columnar microstructure, owing to the high growth rate following the c-axis. However, the incorporation of Fe^{3+} in the ZnO network not only leads to an increase of the c-axis parameter, but in addition a transition of the ZnO grain morphology towards plate-like zincite crystal has been already reported [25].

Such a microstructure for the wurtzite – spinel nanocomposite films is quite different from the regular stacking observed in some nanocomposite films like HfO_2-SiO_2 [37] or YBCO-BZO [38] for example. The formation of such regular multilayer nanocomposite films was assumed to be due to the surface-directed spinodal decomposition (SDSD), based on the preferential attraction of the surface to one of the two components [39]. SDSD simulations show the formation perpendicular to the surface of a composition wave propagating in the film. This leads to the formation of a regular multilayered heteroepitaxial phase assemblage [39]. It must be noticed that the high temperature annealing (1350°C) of a bulk ZnO-Fe_3O_4

material [17], leads via the spinodal decomposition, to a regular nanostructure with alternate layers of wurtzite (Fe rich ZnO) and spinel (Zn rich Fe_3O_4) with an average grain boundary spacing value of about 200 nm [17]. In this case, owing to the high temperature treatment, the diffusion of Fe and Zn is sufficient to form the regular nanostructure.

Even if we have observed a slight enrichment in Fe towards the surface of the nanocomposite films formed at 500°C, it is not possible to conclude that the surface-directed spinodal decomposition process can be at the origin of the microstructure observed in this work. Taking into account the fact that a Zn enrichment appears at the interface between wurtzite and spinel phase (Figures 6 and 7], and that the Zn concentration plays an important role in the in-plane orientation of the spinel phase, a possible explanation of the microstructure observed in this work can be proposed according to the specificity of the PLD growth.

As noted above, the main phase observed in the nanocomposite films is the spinel phase, with the presence of thinner wurtzite platelets. The overall cationic composition of the film determined by RBS is $Zn_{0.27}Fe_{0.73}$, but this is only a mean value. In fact, the PLD can be considered as a random process, in the sense that the flux of the Zn and Fe species coming from the target will not be the same at the same time in all the points of the substrate. Moreover, for a given point of the substrate, the flux of Zn and Fe species will not be the same as a function of time. This means that locally, the Zn and Fe concentrations measurable by EDX technique can be different from the mean values determined by RBS, and will be different as a function of time. As a matter of fact, considering the first step of the film deposition on sapphire substrate, locally a Zn-rich region can exist in some points. If this Zn enrichment is not too large (< 33%) it can be at the origin of the S-30° orientation for the spinel phase (as observed in Figures 6(c) and (d)), by the formation of a Zn-rich spinel phase. On the contrary, if this Zn enrichment is important (about 50%), the formation of the wurtzite

phase at the interface with the Al_2O_3 substrate can occur (as it is shown in Figures 6(a) and (b)). However, this Zn local enrichment cannot occur during all the film growth, and when the Zn concentration decreases, the spinel phase will grow on top of the W-30° crystallite with the S-30° orientation (as shown in Fig. 6(a)).

Similar phenomena can occur inside the film, and the Zn enrichment on top of a spinel S-30° crystallite, will lead to the formation wurtzite W-30° (Fig. 7). Then a decrease of the Zn concentration will lead to the formation of the spinel phase with the S-30° orientation (Fig. 7). If the Zn enrichment locally inside the film is not sufficient to induce the formation of the wurtzite phase, it could lead to a change from S-0° towards S-30° orientation (as shown in Fig. 5). The driving force for the wurtzite-spinel nanocomposite film would thus be the change of composition in the film as a function of the position and of time.

As previously mentioned [20], the nanocomposite epitaxial wurtzite-spinel films based on earth-abundant and low cost materials, presenting both a good optical absorption in a large domain of the solar spectrum, and a noticeable electronic conductivity, could be an interesting approach for photocatalytic applications. The nanocomposite wurtzite-spinel films could also be of interest in thermoelectric applications. In fact, the microstructure observed in this work with a large number of boundaries between the two phases is particularly interesting in view to obtain a low thermal conductivity value [40]. The thermal conductivity of the bulk ZnO-$ZnFe_2O_4$ material presenting alternate layers of wurtzite and spinel with a 200 nm spacing was found around 10 W/mK, i.e. a value 10 times lower than the thermal conductivity of bulk ZnO [17]. Taking into account that the density of boundaries is ten times higher in our nanocomposite wurtzite - spinel film (spacing about 20 nm), we could expect a further decrease of the thermal conductivity down to 1-2W/mK.

In summary, nanocomposite films formed with both wurtzite (Fe:ZnO) and spinel ($Zn:Fe_3O_4$) phases have been grown by PLD on c-cut sapphire substrate. Both phases present

preferential axis growth according to the (0001) wurtzite and (111) spinel planes parallel to the basal (000l) sapphire plane. The wurtzite crystallites are epitaxially grown following to a 30° rotation of the hexagons of the (0001) Fe:ZnO plane with respect to the hexagons of the (0001) Al_2O_3 plane. On the contrary, the spinel crystallites show two main in-plane epitaxial relationships corresponding to the coincidence of spinel and sapphire hexagons without rotation (S-0°), or a 30° rotation between the hexagonal cells (S-30°). In addition, these specific W-30°, S-0° and S-30° in-plane relationships have been also observed for the wurtzite and spinel crystallites inside the film. The presence of S-0° or S-30° orientations for spinel crystallites on the (000l) sapphire planes has been related to the Zn concentration in the (111) family planes of spinel crystallites. The S-30° and S-0° orientations correspond to low and high Zn concentrations in the spinel phase, respectively. This result is tentatively explained by the variation of Zn^{2+} ion concentration in the tetrahedral sites in the 111 triangular planes (Tt plane).

Acknowledgments

X. Portier would like to thank the French ANR (Agence Nationale de la Recherche) institution for the EQUIPEX “GENESIS” grant “ANR-11-EQPX-0020” in the frame of the “Investissements d’avenir” as well as FEDER and the Normandie Region funding that allowed the acquisition and the use of the FIB system (HELIOS Nanolab 600 from FEI) and the EELS spectrometer (QUANTUM ER965 from GATAN). N. Jedrecy thanks the “ANR-15-CE09-0005-01” for their funding and warmly acknowledges D. Demaille for the preliminary TEM analyses conducted on the nanocomposite films. C. Cachoncinlle, E. Millon and J. Perrière would like to thank T. Orlowski for her help during specific manipulations.

References

[1]- H.B. Wu, J.S. Chen, H.H. Hng, X.W. Lou, Nanostructured metal oxide-based materials as advanced anodes for lithium-ion batteries, Nanoscale **4** (2012) 2526-2542.

[2]- D.R. Miller, S.A. Akbar, P.A. Morris, Nanoscale metal oxide-based heterojunctions for gas sensing: A review, Sensors and Actuators B-Chemical **204** (2014) 250-272.

[3]- H. Zheng, J. Wang, S.E. Loftland, Z. Ma, L. Mohaddes-Ardabili, T. Zhao, L. Salamanca-Riba, S.R. Shindle, S.B. Ogale, F. Bai, D. Viehland, Y. Jia, D.G. Schlom, M. Wuttig, A. Roytburd, R. Ramesh, Multiferroic $BaTiO_3$-$CoFe_2O_4$ nanostructures, Science **303** (2004) 661-663.

[4]- E. Millon, M. Nistor, C. Hebert, Y. Davila, J. Perrière, Phase separation in nanocomposite indium tin oxide thin films grown at room temperature: on the role of oxygen deficiency, J. Mat. Chem. **22** (2012) 12179-12185.

[5]- Y. Li, M.F. Jiao, H.J. Zhao, M.J. Yang, High performance gas sensors based on in-situ fabricated ZnO-polyaniline nanocomposite: The effect of morphology on the sensing properties, Sensors and Actuators B-Chemical **264** (2018) 285-295.

[6]- N. Jedrecy, M. Hamieh, C. Hebert, J. Perrière, High magnetoresistance at low magnetic fields in self-assembled ZnO-Co nanocomposite films, Nanoscale **9** (2017)10431.

[7]- V. Corral-Flores, D. Bueno-Baques, R.F. Ziolo, Synthesis and characterization of novel $CoFe_2O_4$-$BaTiO_3$ multiferroic core-shell-type nanostructures, Acta Mater. **58** (2010) 764-769.

[8]- A. Chen, Z.X. Bi, Q.X. Jia, J.L. MacManus-Driscoll, H.Y Wang, Microstructure, vertical strain control and tunable functionalities in self-assembled, vertically aligned nanocomposite thin films, Acta Mater. **61** (2013) 2783-2792.

[9]- J.L. MacManus-Driscoll, Self-Assembled Heteroepitaxial Oxide Nanocomposite Thin Film Structures: Designing Interface-Induced Functionality in Electronic Materials, Adv. Funct. Mater. **20** (2010) 2035-2045.

[10]- J.X. Zhang, Y.L. Li, D.G. Schlom, L.Q. Chen, F. Zavaliche, R. Ramesh, Q.X. Jia, Phase-field model for epitaxial ferroelectric and magnetic nanocomposite thin films, Appl. Phys. Lett. **90** (2007) 052909.

[11]- T. Fix, E. Choi, J.W.A. Robinson, S.B. Lee, A. Chen, B. Prasad, H. wang, M.G. Blamire, J.L. MacManus-Driscoll, Electric-Field Control of Ferromagnetism in a Nanocomposite via a ZnO Phase, Nano Letters **13** (2013) 5886-5890.

[12]- M.A. Woo, T.W. Kim, I.Y. Kim, S.J. Hwang, Synthesis and lithium electrode application of ZnO-$ZnFe_2O_4$ nanocomposites and porously assembled $ZnFe_2O_4$ nanoparticles, Solid State ionics **182** (2011) 91-97.

[13]- F.O. Agyemang, H. Kim, Electrospun $ZnFe_2O_4$-based nanofiber composites with enhanced supercapacitive properties, Mater. Sci. Eng., B **211** (2016) 141-148.

[14]- S.R. Liu, M.Y. Guan, X.Z. Li, Y. Guo, Light irradiation enhanced triethylamine gas sensing materials based on ZnO/$ZnFe_2O_4$ composites, Sens. Actuators B-Chemical **236** (2016) 350-357.

[15]- S. Cho, J.-W. Jang, L.Li, J. Jian, H. Wang, J.L. MacManus-Driscoll, Self-Assembled Heteroepitaxial Oxide Nanocomposite for Photoelectrochemical Solar Water Oxidation, Chem. Mater. **28** (2016) 3017-3023.

[16]- Y. Li, Y.Z. Li, Y. Yin, D. Xia, H. Ding, C. Ding, J. Wu, Y. Yan, Y. Liu, P.K. Wong, A. Lu, Facile synthesis of highly efficient ZnO/$ZnFe_2O_4$ photocatalyst using earth-abundant sphalerite and its visible light photocatalytic activity, Appl. Catal., B **226** (2018) 324-336.

[17]- X. Liang, Thermoelectric Transport Properties of Fe-Enriched ZnO with High-Temperature Nanostructure Refinement, ACS Appl. Mater. Interfaces **7** (2015) 7927-7937.

[18]- S.A. Degterov, E. Jak, P.C. Hayes, A.D. Pelton, Experimental study of phase equilibria and thermodynamic optimization of the Fe-Zn-O system, Metall. Mater. Trans. B **32** (2001) 643-657.

[19]- S.C. Schaefer, R.A. McCune, Eectrochemical determination of thermodynamic properties and X-ray diffraction investigation of the Fe_3O_4-$ZnFe_2O_4$ system, Metall. Mater. Trans. B **17** (1986) 515-521.

[20]- J. Perrière, C. Hebert, M. Nistor, E. Millon, J.J. Ganem, N. Jedrecy, Zn1-xFexO films: from transparent Fe-diluted ZnO wurtzite to magnetic Zn-diluted Fe3O4 spinel, J. Mat. Chem. C **3** (2015) 11239-11249.

[21]- N. Jedrecy, C. Hebert, J. Perrière, M. Nistor, E. Millon, Magnetic and magnetotransport properties of $Zn_xFe_{3-x}O_{4-y}$ thin films, J. Appl. Phys. **116** (2014) 213903.

[22]- K. Brachwitz, T. Böntgen, J. Lenzner, K. Ghosh, M. Lorenz, M. Grundmann, Evolution of magnetization in epitaxial $Zn_{1-x}Fe_xO_z$ thin films ($0 \leq x \leq 0.66$) grown by pulsed laser deposition, J. Phys. D: Appl. Phys. **51** (2018) 245003.

[23]b1- M. Morcrette, A. Gutierrez-Llorente, W. Seiler, J. Perrière, A. Laurent, P.Barboux , Epitaxial growth of Pt and oxide multilayers on MgO by laser ablation, J. Appl. Phys. **88** (2000) 5100-5106.

[24]- S. Zhou, K. Potzger, H. Reuther, G. Talut, F. Eichhorn, J. von Borany, W. Skorupa, M. Helm, J. Fassbender, Crystallographically oriented magnetic $ZnFe_2O_4$ nanoparticles synthesized by Fe implantation into ZnO, J. Phys. D : Appl. Phys. **40** (2007) 964-969.

[25]- T. Yamashita, R. Hansson, P.C. Hayes, The relationships between microstructure and crystal structure in zincite solid solutions, J. Mater. Sci. **41** (2006) 5559-5568.

[26]- I. Ohkubo, Y. Matsumoto, A. Ohtomo, T. Ohnishi, A. Tsukazaki, M. Lippmaa, H. Koinuma, M. Kawasaki, Investigation of ZnO/sapphire interface and formation of ZnO nanocrystalline by laser MBE, Appl. Surf. Sci. **159-160** (2000) 514-519.

[27]- V. Craciun, R.K. Singh, J. Perrière, J. Spear, D. Craciun, Epitaxial ZnO films grown on sapphire (001) by ultraviolet-assisted pulsed laser deposition, J. Electrochem. Soc. **147** (2000) 1077-1079.

[28]- J. Narayan, K. Dovodenko, A.K. Sharma, S. Oktyabrsky, Defects and interfaces in epitaxial ZnO/alpha-Al_2O_3 and AlN/ZnO/alpha-Al_2O_3 heterostructures, J. Appl. Phys. **84** (1998) 2597-2601.

[29]- J. Narayan, Recent progress in thin film epitaxy across the misfit scale (2011 Acta Gold Medal Paper), Acta Mater. **61** (2013) 2703-2724.

[30]- N. Sbai, J. Perrière, W. Seiler, E. Millon, Epitaxial growth of titanium oxide thin films on c-cut and alpha-cut sapphire substrates, Surf. Sci. **601** (2007) 5649-5658.

[31]- K. Fitzner, Thermodynamic properties and cation distribution of the $ZnFe_2O_4$- Fe_3O_4 spinel solid-solutions at 900°C, Thermochimica Acta **31** (1979) 227-236.

[32]- W. Seiler, M. Nistor, C. Hebert, J. Perrière, Epitaxial undoped indium oxide thin films: Structural and physical properties, Solar En. Mat. Solar Cells **116** (2013) 34-42.

[33]- V.G. Harris, N.C. Koon, C.M. Williams, Q. Zhang, M. Abe, Cation distribution in NiZn-ferrite films determined using x-ray absorption fine structure, J. Appl. Phys.**79** (1996) 4561-4563.

[34]- X.G. Wang, J.R. Smith, M. Scheffler, Effect of hydrogen on Al2O3/Cu interfacial structure and adhesion, Phys. Rev. B **66** (2002) 073411.

[35]- H. Yahiro, H. Tanak, Y. Yamamoto, T. Kawai, Growth mode of (111) oriented spinel type $ZnFe_2O_4$ thin film by laser-molecular beam epitaxy technique, Solid State Comm. **123** (2002) 535-538.

[36]- X. Liu, D. Choudhury, Y. Cao, S. Middey, M. Kareev, D. Meyers, J.-W. Kim, P. Ryan, J. Chakhalian, Epitaxial growth of (111)-oriented spinel $CoCr_2O_4/Al_2O_3$ heterostructures, Appl. Phys. Lett. **106** (2015) 071603.

[37]- J. Liu, X. Wu, W.N. Lennard, D. Landheer, Surface-directed spinodal decomposition in hafnium silicate thin films, Phys. Rev. B **80** (2009) 041403(R)

[38]- H. Yang, H. Wang, B. Maiorov, J. Lee, D. Talbayev, M.J. Hinton, D.M. Feldmann, J.L. MacManus-Driscoll, A.J. Taylor, L. Civale, T.R. Lemberger, Q.X. Jia, Self-assembled multilayers and enhanced superconductivity in $(YBa_2Cu_3O_{7-x})(0.5)$: $(BaZrO_3)(0.5)$ nanocomposite films , J. Appl. Phys. **106** (2009) 093914.

[39]- S. Puri, K. Binder, Surface effects on spinodal decomposition in binary-mixtures and the interplay with wetting phenomena, Phys Rev. E **49** (1194) 5359-5377.

[40]- X. Liang, D.R. Clarke, Relation between thermoelectric properties and phase equilibria in the ZnO-In_2O_3 binary system, Acta Mater. **63** (2014) 191-201.

Table captions

Table I: Matching orientation relationships, lattice mismatch δ and size of epitaxial domain D, for the various epitaxial configurations evidenced in this work. The m, p and D values are given with respect to the mentioned directions and the lattice mismatch is calculated with respect to the substrate or the template layer.

Figure captions

Fig. 1: Typical RBS spectrum for a nanocomposite film grown on c-cut sapphire substrate at 500°C and 5 10^{-7} mbar residual pressure. The solid line is the simulated spectrum obtained by the use of the RUMP program.

Fig. 2: (a) Bright field TEM image of the Zn-Fe-O film. Contrasts in the image are due to Bragg contrast and/or composition of the grains. (b) STEM HAADF dark field image with the corresponding Zn (c), O (d) and Fe (e) chemical maps obtained by STEM EDX.

Fig. 3: θ-2θ diffraction patterns recorded on nanocomposite (wurtzite and spinel phases) films grown at 500°C under residual vacuum (10^{-7} mbar). The vertical dashed lines figure the bulk positions.

Fig. 4: Pole figures recorded on a nanocomposite ($Zn_{0.27}Fe_{0.73}O_{1.33}$) film for (a) the wurtzite phase and the (10-11) reflection (2θ = 36.25°); (b) the spinel phase and the (220) reflection (2θ = 29.8°).

Fig. 5: HRTEM image of a region showing the different orientations of wurtzite and spinel grains with respect to the substrate.

Fig. 6: (a) HRTEM image and (b) EDX profile of S-30 oriented spinel at the bottom of the film. (c) HRTEM image and (d) EDX profile of S-0 oriented spinel at the bottom of the film. The EDX profiles have been recorded along a 60 nm line from the film towards the substrate in both cases. The interfacial region rich in Zn of the S-0° spinel is delimited by dashed lines in (d).

Fig. 7: (a) HRTEM image and (b) EDX profile of S-0 oriented spinel and W-30 oriented wurtzite at the bottom of the film (recorded from the film towards the substrate as indicated by the arrow in (a)). (c) STEM HAADF dark field image of two S-30 and S-0 oriented spinel grains separated by a W-30 oriented wurtzite crystallite, (d) EDX profile across the three grains recorded from the top to the bottom of the region as indicated by the arrow in (b). The interfacial regions rich in Zn are delimited by dashed lines in (b) and (d).

Table I

Epitaxial relationships	Matching relationships	Mismatch δ Domain size D
W-30° on sapphire ***Fe:ZnO [10-10] // Al_2O_3 [2-1-10]*** ***Fe:ZnO [2-1-10] // Al_2O_3 [10-10]***	m = 7 p = 6 m = 2 p = 5	δ = 1.41 % D = 34 Å δ = - 1.41 % D = 16 Å
S-30° on sapphire ***Zn:Fe_3O_4 [10-1] // Al_2O_3 [10-10]***	m = 5 p = 7	δ = 0.9 % D = 42 Å
S-0° on sapphire ***Zn:Fe_3O_4 [10-1] // Al_2O_3 [2-1-10]***	m = 5 p = 4	δ = - 0.15 % D = 24 Å
S-11° on sapphire ***Zn:Fe_3O_4 [11-2] // Al_2O_3 [41-50]***	m = 5 p = 6	δ = - 1.9 % D = 62 Å
S-0° on wurtzite W-30° ***Zn:Fe_3O_4 [11-2] // Fe:ZnO [2-1-10]***	m = 19 p = 6	δ = - 0.05 % D = 62 Å
W-30° on spinel S-30° ***Fe:ZnO [2-1-10] // Zn:Fe_3O_4 [10-1]***	m = 6 p = 11	δ = 0.3 % D = 36 Å
S-30° on spinel S-0° ***Zn:Fe_3O_4 [10-1] // Zn:Fe_3O_4 [11-2]***	m = 4 p = 7 m = 19 p = 11	δ = 1 % D = 42 Å δ = 0.3 % D = 114 Å

Table I: Matching orientation relationships, lattice mismatch δ and size of epitaxial domain D, for the various epitaxial configurations evidenced in this work. The m, p and D values are given with respect to the mentioned directions and the lattice mismatch is calculated with respect to the substrate or the template layer.

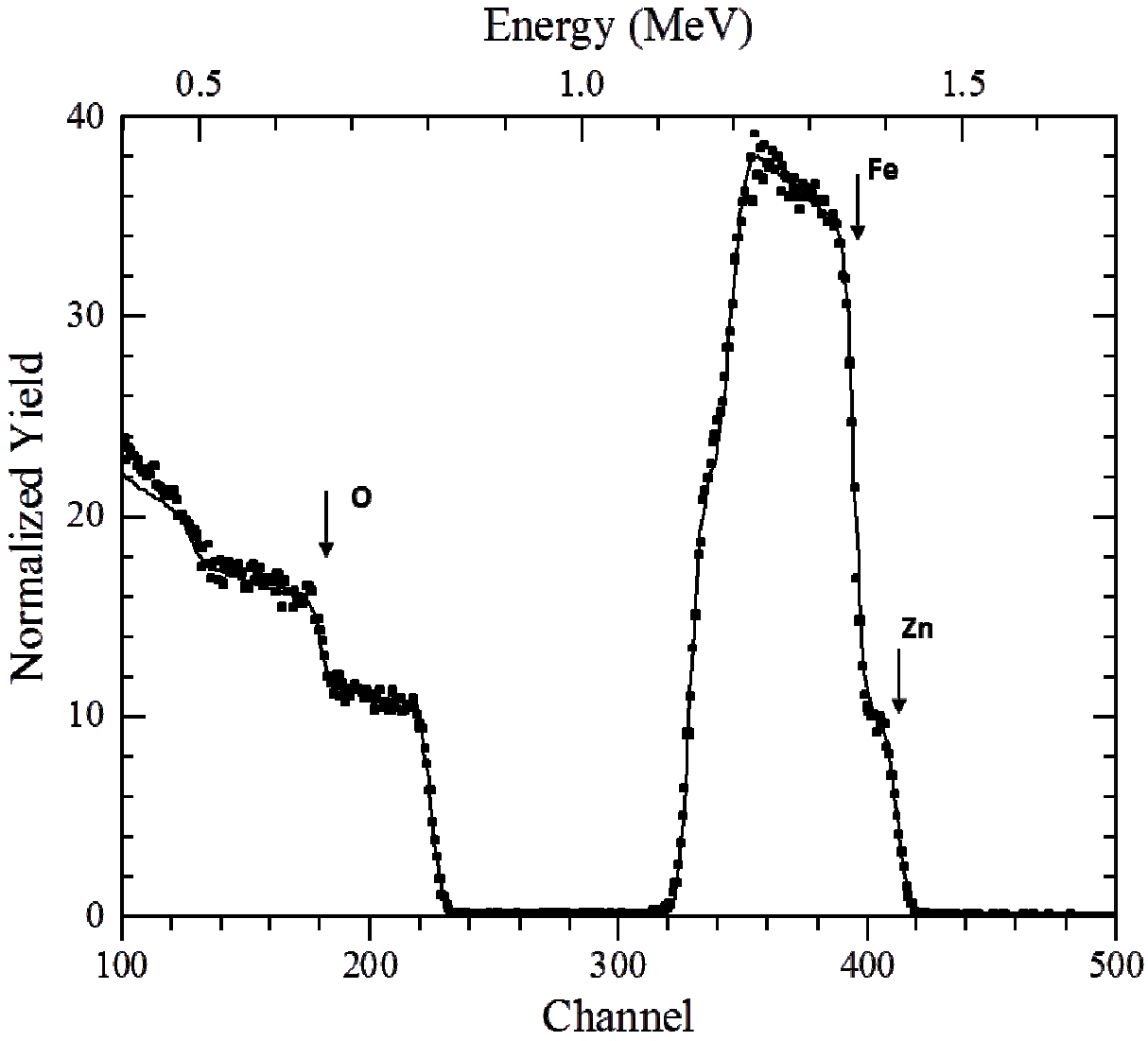

Fig. 1: Typical RBS spectrum for a nanocomposite film grown on c-cut sapphire substrate at 500°C and 5 10^{-7} mbar residual pressure. The solid line is the simulated spectrum obtained by the use of the RUMP program.

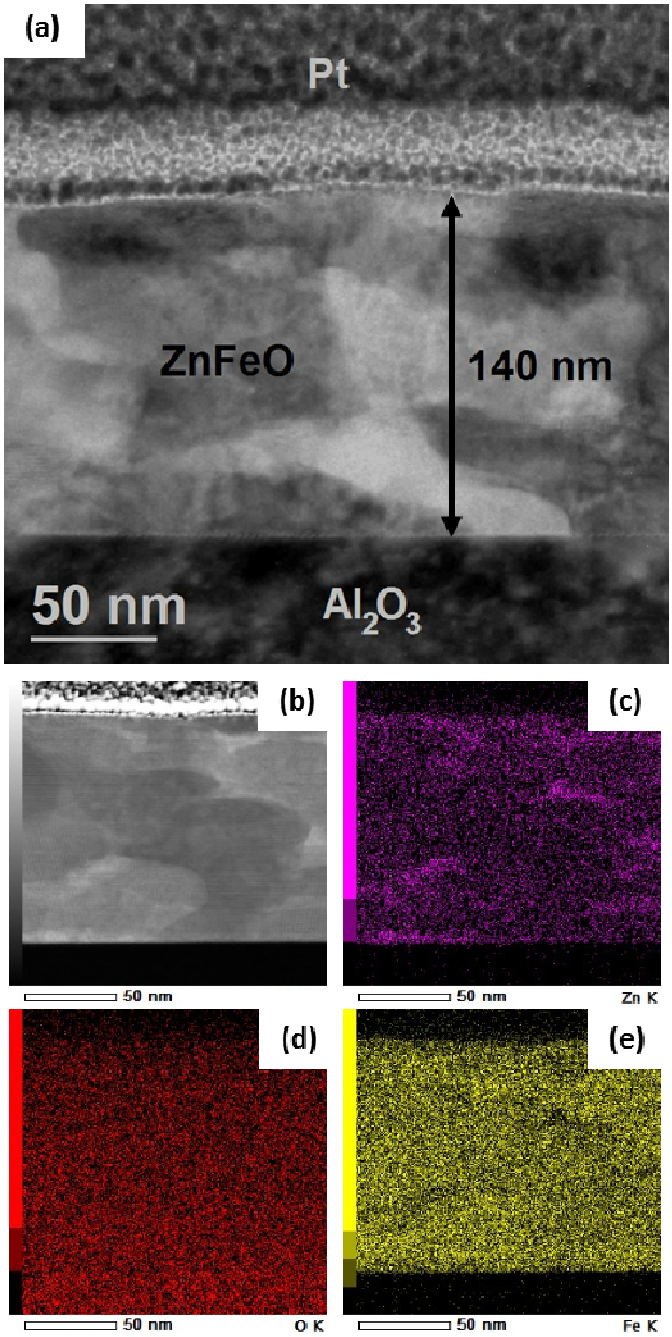

Fig. 2: (a) Bright field TEM image of the Zn-Fe-O film. Contrasts in the image are due to Bragg contrast and/or composition of the grains. (b) STEM HAADF dark field image with the corresponding Zn (c), O (d) and Fe (e) chemical maps obtained by STEM EDX.

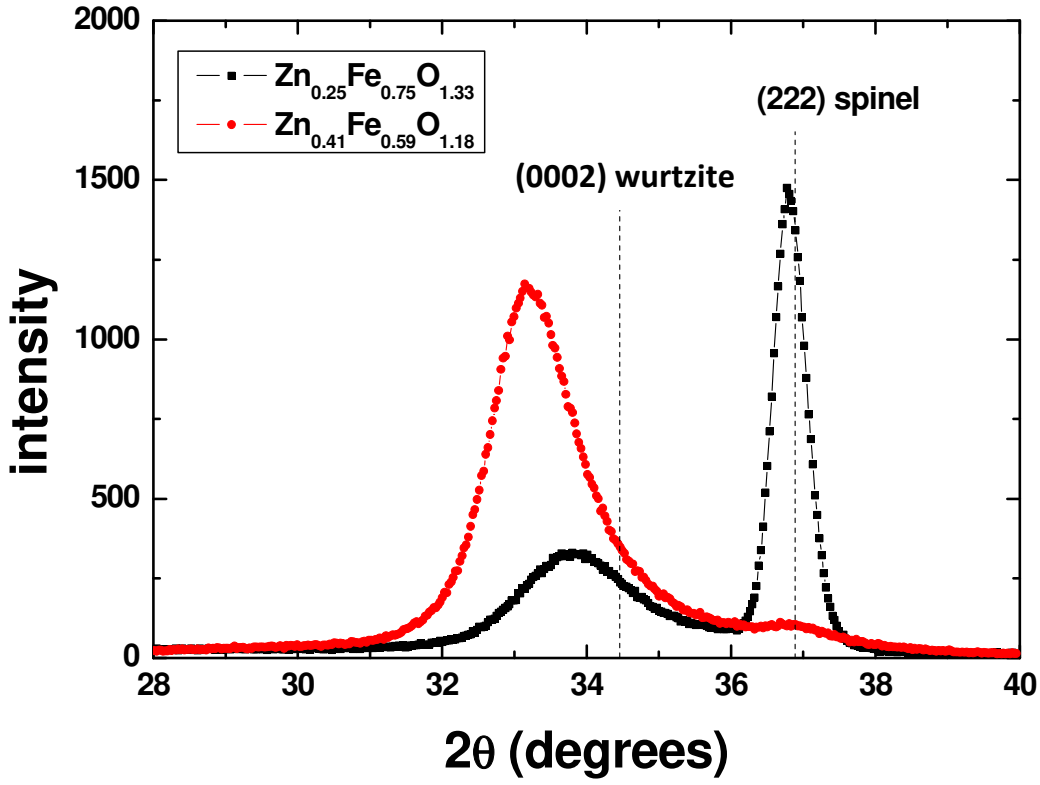

Fig. 3: θ-2θ diffraction patterns recorded on nanocomposite (wurtzite and spinel phases) films grown at 500°C under residual vacuum (10^{-7} mbar). The vertical dashed lines figure the bulk positions.

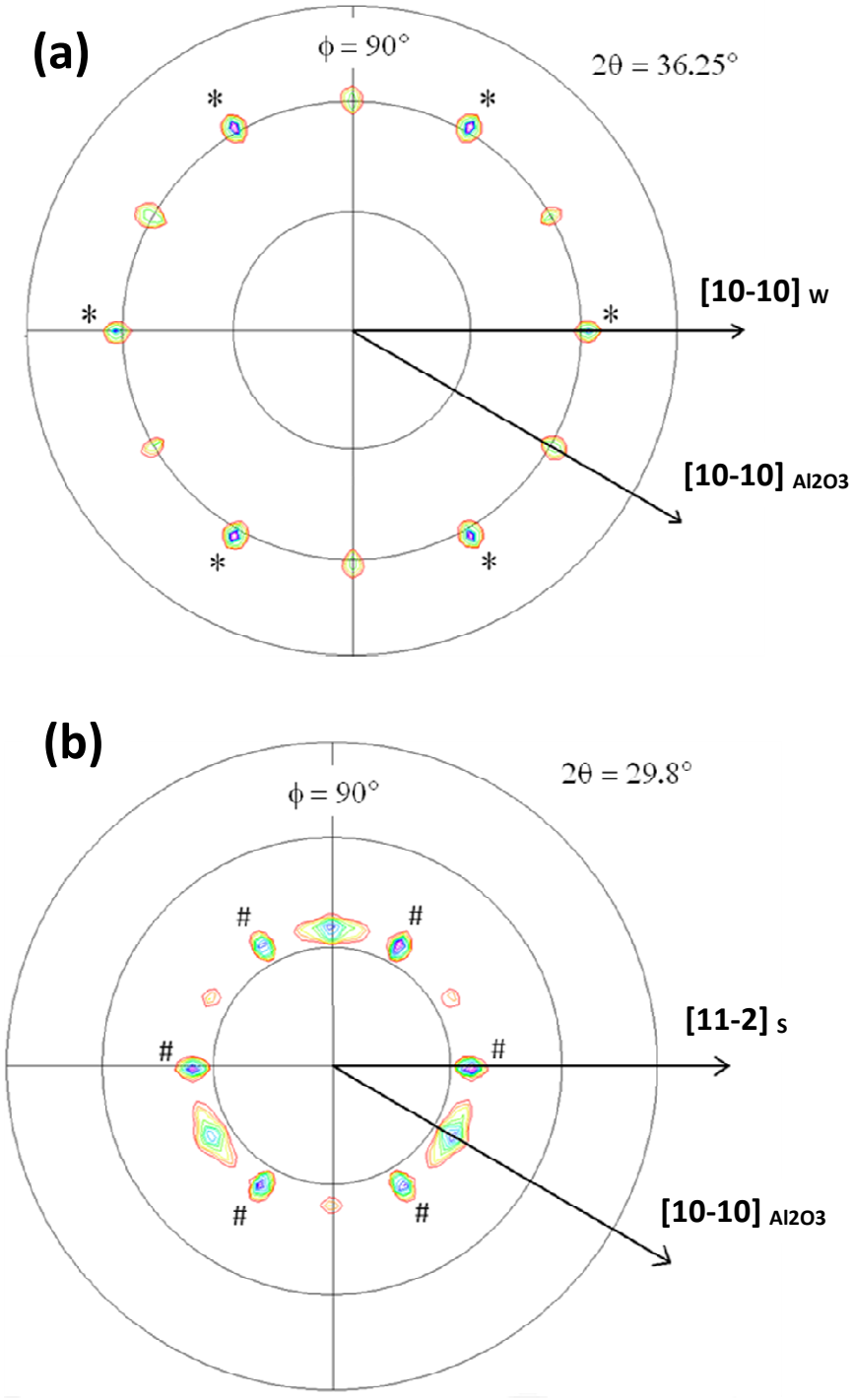

Fig. 4: Pole figures recorded on a nanocomposite ($Zn_{0.27}Fe_{0.73}O_{1.33}$) film for (a) the wurtzite phase and the (10-11) reflection (2θ = 36.25°); (b) the spinel phase and the (220) reflection (2θ = 29.8°).

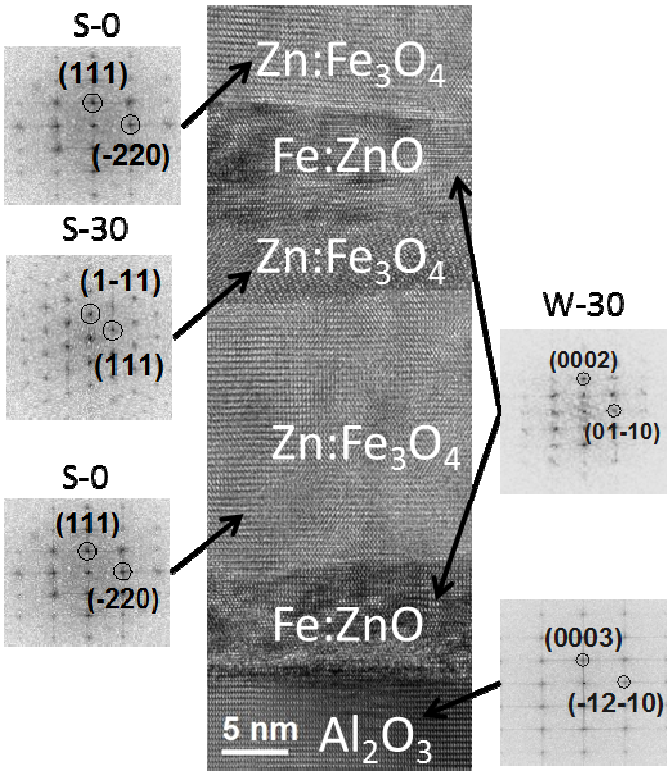

Fig. 5: HRTEM image of a region showing the different orientations of wurtzite and spinel grains with respect to the substrate.

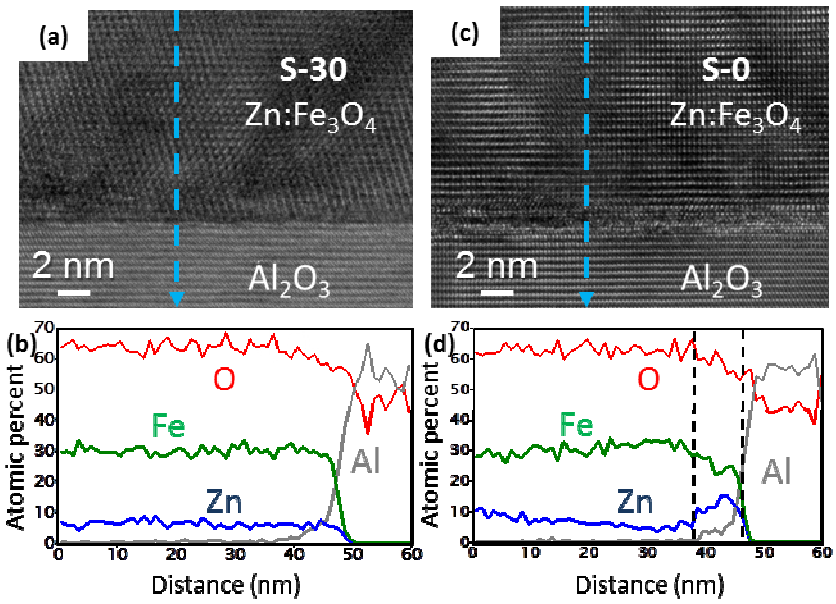

Fig. 6: (a) HRTEM image and (b) EDX profile of S-30 oriented spinel at the bottom of the film. (c) HRTEM image and (d) EDX profile of S-0 oriented spinel at the bottom of the film. The EDX profiles have been recorded along a 60 nm line from the film towards the substrate in both cases. The interfacial region rich in Zn of the S-0° spinel is delimited by dashed lines in (d).

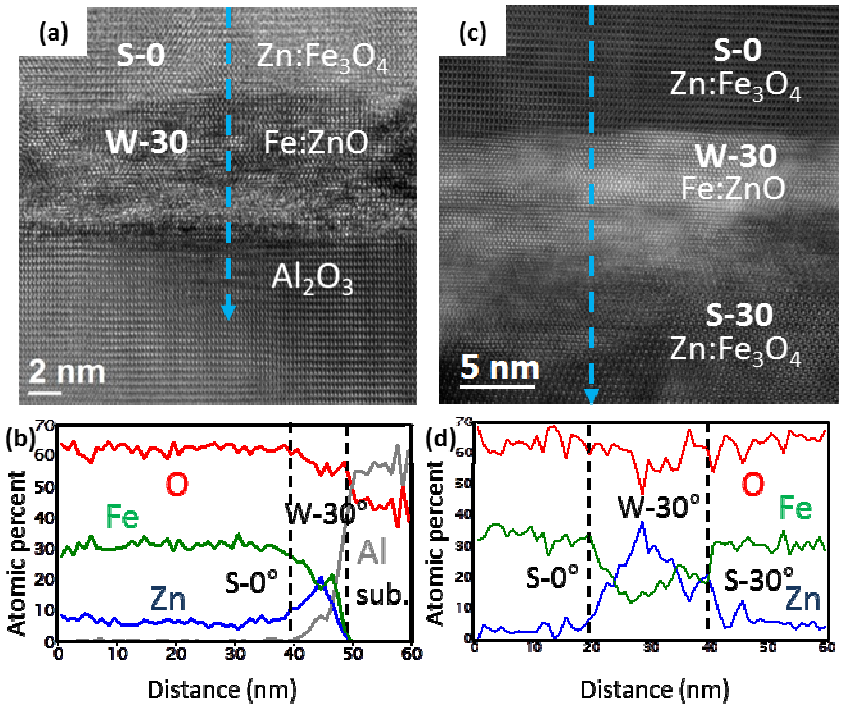

Fig. 7: (a) HRTEM image and (b) EDX profile of S-0 oriented spinel and W-30 oriented wurtzite at the bottom of the film (recorded from the film towards the substrate as indicated by the arrow in (a)). (c) STEM HAADF dark field image of two S-30 and S-0 oriented spinel grains separated by a W-30 oriented wurtzite crystallite, (d) EDX profile across the three grains recorded from the top to the bottom of the region as indicated by the arrow in (c). The interfacial regions rich in Zn are delimited by dashed lines in (b) and (d).

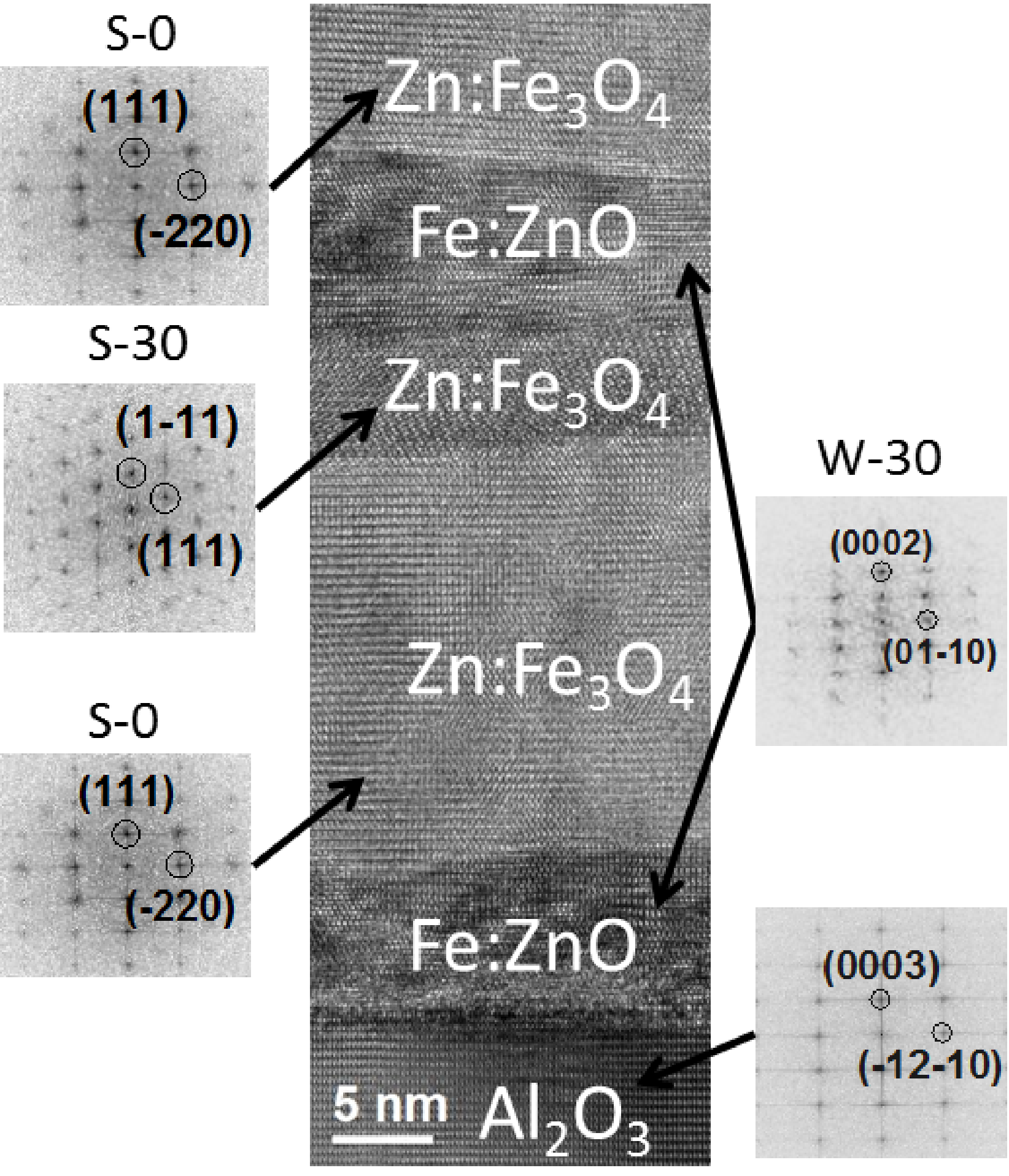
S-0
(111)
(-220)
S-30
(1-11)
(111)
S-0
(111)
(-220)
Zn:Fe3O4
Fe:ZnO
Zn:Fe3O4
Zn:Fe3O4
Fe:ZnO
5 nm
Al2O3
W-30
(0002)
(01-10)
(0003)
(-12-10)